Reprinted from JOURNAL OF APPLIED METEOROLOGY, Vol. 34, No. 2, February 1995
American Meteorological Society

Considerations for Modeling Thin Cirrus Effects via Brightness Temperature Differences

E. O. SCHMIDT AND R. F. ARDUINI

Lockheed Engineering and Science Co., Hampton, Virginia

B. A. WIELICKI

Atmospheric Sciences Division, NASA Langley Research Center, Hampton, Virginia

R. S. STONE

Cooperative Institute for Research in Environmental Sciences, University of Colorado, Boulder, Colorado

S.-C. TSAY

Department of Meteorology, University of Maryland, College Park, Maryland

(Manuscript received 29 November 1993, in final form 22 March 1994)

ABSTRACT

Brightness temperature difference (BTD) values are calculated for selected Geostationary Operational Environmental Satellite (*GOES-6*) channels (3.9, 12.7 μm) and Advanced Very High Resolution Radiometer channels (3.7, 12.0 μm). Daytime and nighttime discrimination of particle size information is possible given the infrared cloud extinction optical depth and the BTD value. BTD values are presented and compared for cirrus clouds composed of equivalent ice spheres (volume, surface area) versus randomly oriented hexagonal ice crystals. The effect of the hexagonal ice crystals is to increase the magnitude of the BTD values calculated relative to equivalent ice sphere (volume, surface area) BTDs. Equivalent spheres (volume or surface area) do not do a very good job of modeling hexagonal ice crystal effects on BTDs; however, the use of composite spheres improves the simulation and offers interesting prospects. Careful consideration of the number of Legendre polynomial coefficients used to fit the scattering phase functions is crucial to realistic modeling of cirrus BTDs. Surface and view-angle effects are incorporated to provide more realistic simulation.

1. Introduction

Current efforts in the remote sensing of clouds via satellite-, aircraft-, and ground-based sensors hinge on the comparison of theoretical model results and radiometric data. These comparisons provide validation of the modeling techniques and the physics of the problem studied. Discrepancies indicate limitations of the sensors, theoretical or physical assumptions and limitations, and/or numerical inadequacies of the model assumptions and technique used.

For the problem of thin cirrus clouds, either single layer or in conjunction with lower-level clouds, there are many complexities involved. Remote sensing of thin cirrus via satellites has led to attempts to derive optical and microphysical properties. Parameters most commonly derived include cloud optical depth, effective particle size, cloud fraction, cloud-top temperature, cloud-top height, and emissivity. Analytic methods used to derive this information include spatial coherence (Coakley and Bretherton 1982), texture techniques (Welch et al. 1988), and many bispectral or multispectral techniques (Platt 1983; Rossow et al. 1985; Minnis et al. 1987; Baum et al. 1992). Stone et al. (1990) suggest a bispectral method that is based on the combined analysis of lidar/radiometric (LIRAD) data (Platt and Dilley 1979) and radiosonde data, employing a radiative transfer model. Stone et al. (1990) compare two independent estimates of cloud properties: one estimate is derived from a LIRAD analysis and radiosonde data, and the second estimate is derived from a difference between coincident infrared (IR) and near-IR (NIR) measurements.

The goal of this paper is to address the application of brightness temperature differences (BTDs) to remote sensing of cloud properties, such as those suggested by Stone et al. (1990), Prabhakara et al. (1988), Inoue (1987), and others. We study the parameters that affect BTDs, with particular attention toward a physically realistic scenario: high, thin cirrus composed of hexagonal ice crystals over a nonblack surface. The sensitivity of the radiative transfer model to the number

Corresponding author address: Dr. E. O. Schmidt, The Analytic Science Corp., 55 Walkers Brook Drive, Reading, MA 01867. E-mail: eoschmidt@tasc.com

of terms in the Legendre expansion of the scattering phase functions is also evaluated. We present examples of the errors produced by Legendre polynomial fits to truncated and untruncated phase functions, along with the effects of view angle, ice crystal size, equivalent or composite ice sphere approximations, and a nonblack Lambertian surface on the NIR–IR BTD as seen by a satellite looking at a thin cirrus cloud above a land (or ocean) surface.

2. BTD simulation

a. Radiative transfer model considerations

The discrete ordinate radiative transfer (DISORT) model code of Stamnes et al. (1988) was used to perform the calculations to theoretically simulate the effects of thin cirrus. This model has been used by a number of researchers (Schmidt 1991; Tsay et al. 1991; Stephens and Tsay 1990), and the results presented in Fig. 1 (see section 2c discussion) compare precisely with those obtained from the adding–doubling models used by Stone et al. (1990) and others (Minnis 1992, personal communication). All BTD calculations performed for this paper were done with DISORT.

b. Cloud model

For radiative transfer modeling of thin cirrus, the simplest approach is to treat the cloud particles as ice spheres with an assumed size distribution. A Mie scattering code (Wiscombe 1979) is then used to determine the optical properties of the ice sphere distribution for the theoretical models. Given the highly complex nature of cirrus microphysical properties, this is a reasonable first-order approach. We assumed the cirrus was composed of ice spheres with a gamma size distribution as per Hansen (1971) and used the Mie code to derive the single-scatter albedos, asymmetry factors, volume extinction coefficients, and scattering phase functions for the central wavelengths of the Geostationary Operational Environmental Satellite (*GOES-6*) and Advanced Very High Resolution Radiometer (AVHRR) IR and NIR channels. The calculations were performed for a single, horizontally homogeneous cloud over a black (nonreflective) surface with no intervening atmosphere. We assumed an isothermal cloud temperature of 245 K, a surface temperature of 289 K, a satellite view zenith angle of 37° (0° view azimuth), and a solar zenith angle of 24°. The incident solar intensity used for the 3.9-μm *GOES-6* NIR channel is 1.87 W m^{-2} sr^{-1} (Iqbal 1983, Table C.1).

c. Model results for GOES VAS

Figure 1 shows the daytime and nighttime *GOES-6* VISSR (Visible–Infrared Spin Scan Radiometer) Atmospheric Sounder (VAS) BTDs for cirrus clouds composed of ice spheres with radii R_e of 4, 16, and 64

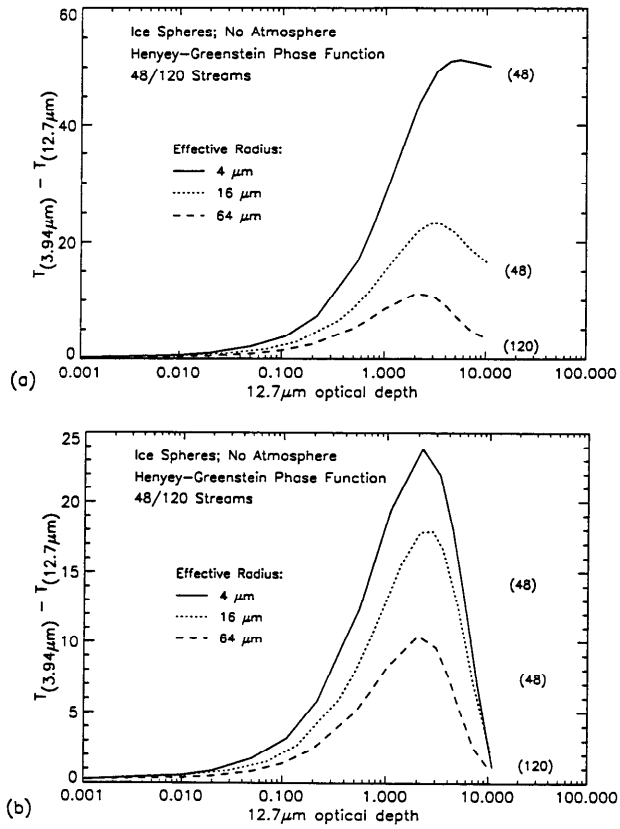

FIG. 1. (a) Daytime and (b) nighttime *GOES-6* VAS BTD signatures ($T_{3.9} - T_{12.7}$) for cirrus composed of ice spheres over a black surface with no intervening atmosphere. Effective radii and the number of streams used in the calculations are shown. A Henyey–Greenstein phase function was used.

μm. Radius R_e is the effective radius of the gamma size distribution that has an effective variance of 0.1. The optical properties were derived with the Mie code, and a Henyey–Greenstein scattering phase function is used. The brightness temperature difference between the NIR and IR channels is defined as BTD = $T_{\mathrm{NIR}} - T_{\mathrm{IR}}$. For the GOES VAS channels, BTD = $T_{3.9} - T_{12.7}$. The contrast between BTD values for small versus large particles (R_e = 4 versus 64 μm) may be used to determine microphysical properties of clouds, provided that the IR optical depth is known. This small to large particle contrast and the BTD magnitude, larger for daytime BTDs due to the NIR reflection of solar radiation, will be referred to as a diurnally dependent BTD signature.

While attempting to duplicate the results of Stone et al. (1990), an error in cloud extinction optical depth wavelength scaling was discovered in their calculation of BTDs for the VAS channels. The correctly scaled results are shown in Fig. 1 for the day and night BTD simulation. Even though the small (4 μm) to large (64 μm) particle contrast was decreased by approximately 25% from the original estimate, it is still significant.

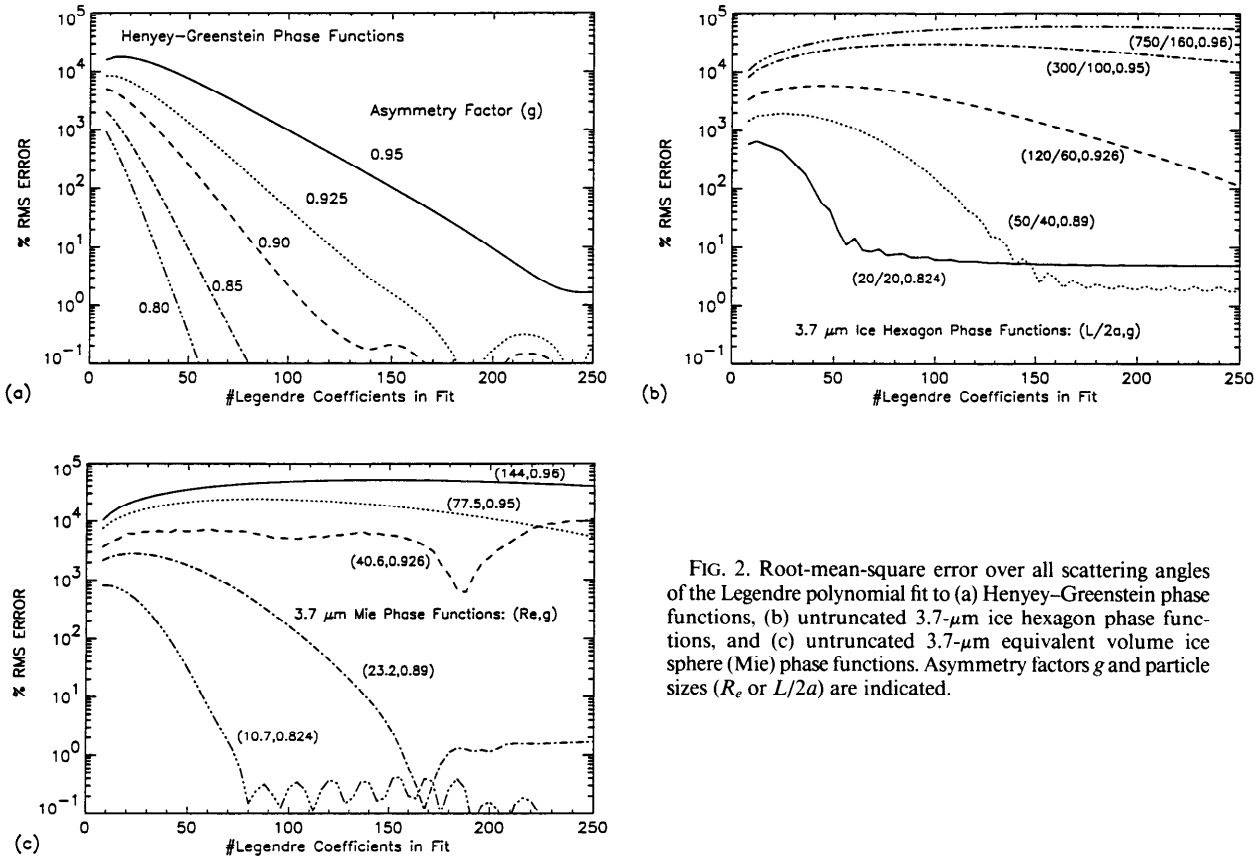

FIG. 2. Root-mean-square error over all scattering angles of the Legendre polynomial fit to (a) Henyey–Greenstein phase functions, (b) untruncated 3.7-μm ice hexagon phase functions, and (c) untruncated 3.7-μm equivalent volume ice sphere (Mie) phase functions. Asymmetry factors g and particle sizes (R_e or $L/2a$) are indicated.

Stone et al. (1990) used single values of refractive index to determine the optical properties for the central wavelengths of each VAS channel. The calculations performed for the VAS channel BTDs shown in Fig. 1 used single wavelength refractive indices. For an exact comparison with the calculations of Stone et al. (1990), the 3.9-μm optical properties used to calculate BTD values in Fig. 1 were taken from Table 2 of their paper. While the single value assumption is valid for the 10.8- and 12.7-μm channels, the variability of the refractive index of ice over the 3.7- and 3.9-μm channels is significant. In subsequent BTD calculations for the AVHRR channels, we used a five-point sensor response weighted average for the 3.7-μm channel (NIR) but single wavelength refractive indices for the 10.8- and 12.0-μm channel (IR). The five-point weighted average generally produced about 10% change in the single-scatter albedo.

3. Theoretical considerations

a. Legendre fit phase functions

Radiative transfer models often use a Legendre polynomial expansion fit to the scattering phase function. Problems arise, however, when the number of terms (Legendre coefficients) used in the expansion produces a fit that does not adequately describe the scattering behavior. This problem is most severe for radiance calculations involving optically thin clouds composed of nonspherical ice crystals as forward scattering is dominant.

The number of Legendre coefficients required to accurately represent a phase function depends on the delta-function behavior of the forward-scattering peak and the complexity of the phase function. Sharply peaked phase functions, such as those determined for hexagonal ice crystals (Takano and Liou 1989), require many terms. This represents a delta-function "class" of phase functions. A second class of phase functions are those that are not well represented by delta functions—for example, those with asymmetry factor $g \leqslant 0.8$. Henyey–Greenstein phase functions fall into both categories (depending on the value of g), as do the so-called Mie phase functions. Both phase function classes may require a significant number of terms in the Legendre expansion to accurately represent them.

Figure 2 shows the relation between the number of terms in the Legendre polynomial fit of phase functions and the rms error over all scattering angles. Figures 2a–c show results for Henyey–Greenstein, 3.7-μm ice hexagon ($L/2a = 20/20$), and 3.7-μm equivalent volume ice sphere (Mie) phase functions, respectively.

TABLE 1. Optical properties of hexagonal ice crystals.[a]

Aspect ratio $L/2a$ (μm/μm)	C_{ext}[b] (μm^2)	ω_0[c] 3.73 μm	ω_0[c] 10.82 μm	ω_0[c] 12.0 μm	R_e (μm) Volume[d]	R_e (μm) Surface area[e]
20/20	859.81	0.8382	0.5726	0.5404	10.7	11.7
50/40	4039.2	0.7263	0.5385	0.5308	23.2	25.4
120/60	13 138.3	0.6671	0.5316	0.5301	40.6	45.7
300/100	51 495.2	0.6064	0.5301	0.5300	77.5	90.5
750/160	196 627.7	0.5656	0.5300	0.5300	144	177

[a] Reference Takano and Liou (1989); Takano et al. (1992).
[b] Large particle extinction cross section.
[c] Single-scatter albedo for ice hexagons.
[d] Equivalent volume effective radius [Eq. (3)].
[e] Equivalent surface area effective radius [Eq. (4)].

Takano and Liou (1989) derived scattering phase functions for a limited set of randomly oriented hexagonal ice crystal sizes at a visible wavelength (0.55 μm). This work has continued (Minnis et al. 1993), and the scattering phase functions for 3.7 and 10.8 μm have been calculated. Crystal sizes are defined by aspect ratio $L/2a$ (length over twice the hexagonal base radius). The aspect ratios and equivalent volume radii are given in Table 1, discussed further in section 2d, and noted (with asymmetry factor g) in the figures. All three phase function fits in Fig. 2 show a decrease in the rms error over all scattering angles with asymmetry factor (or particle size/aspect ratio, as noted). The oscillatory behavior seen is a feature common to all of the curves generated because of the mathematics of the solution, for example, the inability of a series of sines and cosines to reproduce discontinuities in the scattering intensity curves. Large particles (high g values) still require a significant number (even thousands) of terms to produce accurate fits.

b. *Phase function truncation*

A technique commonly used to overcome the problem of strongly peaked phase functions is truncation (Potter 1970; Wiscombe 1977). The basic tenet of phase function truncation is the removal of the sharp forward-scattering peak, followed by a renormalization of the phase function to ensure energy conservation. A Legendre polynomial fit to the modified phase function generally requires fewer terms, especially for the delta-function class of phase functions. Since the fraction of the energy (the truncation fraction) in the forward peak is now considered transmitted radiation, the optical depth and single-scatter albedos of the particles must be scaled proportionately. The technique of scaling the optical properties is based on the similarity method of Sobolev (1978). We performed manually the truncation and renormalization for the phase functions. The scattering angle where the phase function is truncated is called the "truncation angle." While the truncation angle is generally between 0° and 15°, it is sometimes necessary to truncate the phase function to a scattering angle of approximately 30°. In the case of such severe truncation, a significant portion of the forward-scattering behavior is lost. For the modeling performed for this study, we found that truncation angles less than approximately 20° were satisfactory.

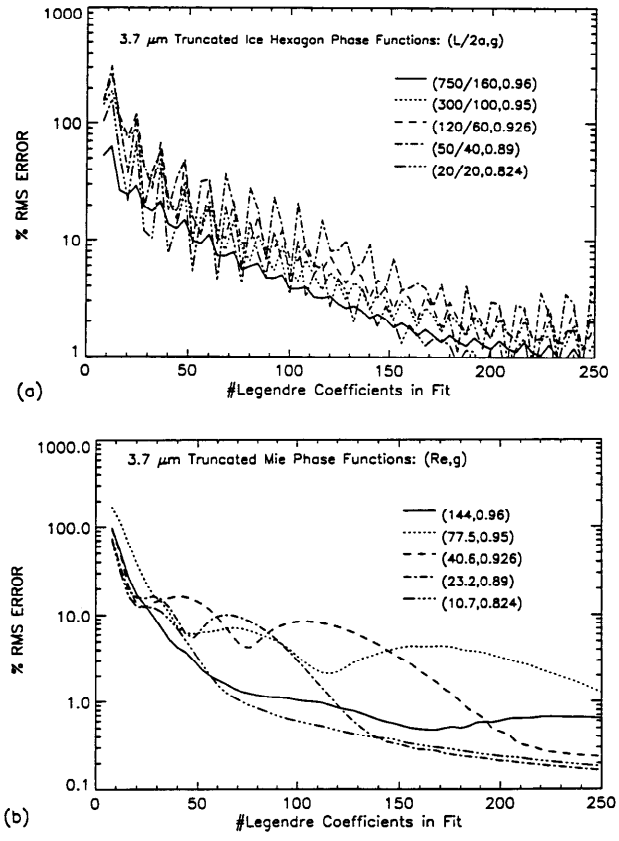

FIG. 3. Root-mean-square error over all scattering angles of the Legendre polynomial fit to (a) truncated 3.7-μm ice hexagon phase functions and (b) truncated 3.7-μm equivalent volume ice sphere (Mie) phase functions. Asymmetry factors g and particle sizes (R_e or $L/2a$) indicated.

Figures 3a,b demonstrate the improvement in the rms error of the Legendre fit versus the number of terms for truncated 3.7-μm ice hexagon and ice sphere phase functions. The same line styles are used in Figs. 3a,b and Figs. 2b,c to denote the rms error for different particle sizes (aspect ratios) with the asymmetry factor annotated. Improved Legendre fits are common for all particle sizes, but the most dramatic improvements are observed for the largest particles (high g values). As particle size increases with respect to wavelength, the forward-scattering intensity increases in magnitude; hence, the delta function nature of the scattering phase function becomes more severe. Therefore, truncation dramatically affects the ability to fit the large particle phase functions with a series of Legendre polynomials. The oscillations in the fits are caused by the discontinuities in the truncated phase functions and the mathematical nature of fitting these "edges" by a series of sines and cosines.

Since scattering is of secondary importance for IR modeling of large particle effects, there is a trade-off between the number of Legendre coefficients used and the acceptable rms error of the fit. Care must be taken, however, to address the relative error in the Legendre fit of the phase function at specific scattering angles of interest. For the delta-function class of phase functions, Legendre polynomial fits to truncated versions of the phase functions with approximately 50 terms typically produce rms errors over all scattering angles of less than approximately 20%.

It is important to note that the scattering geometry between the sun and the National Oceanic and Atmospheric Administration satellites typically provides scattering angles η between 75° and 180°. Hence, it is not necessary to precisely fit the halo angles, and a reasonable fit for η can be performed with only 32 terms, even though the rms error over all angles is rather high. Though a substantial reduction in computational effort and time results, generally it is not sufficient to use this "lower-order" fit without first checking the relative error at the computational angles of interest.

c. *Error in brightness temperature*

The version of the DISORT model code used for these simulations (Stames et al. 1988) sets the number of Legendre coefficients used to fit the phase function identical to the number of streams. The number of streams used to calculate the GOES VAS BTD curves in Fig. 1 varies between 48 and 120, as noted. Untruncated Henyey–Greenstein phase functions were used for the calculations. For daytime simulation, the larger particles (64 μm) required at least twice as many terms as the 4- and 16-μm particles (120 streams versus 48) to ensure convergence of the discrete ordinate solution and reasonable rms errors ($\leq$3%) in the Legendre fit over all scattering angles. Convergence tests were performed for all of the simulations presented in this paper and the minimum number of streams determined for computational efficiency (change in BTD $\leq$ 0.5 K was used as a sufficient condition).

Figure 4 indicates the effects of the number of terms in the Legendre expansion of the scattering phase function on brightness temperature calculations for a specific geometry and two particle sizes. The rms relative error over a range of cloud optical depths (δ_c = 0–10) for a 37° view angle (0° view azimuth) is shown for 3.7 μm. The rms errors shown are relative to the 120-stream calculated values. The 3.7-μm calculations are more sensitive to the number of Legendre coefficients used to fit the phase function than the 10.8- or 12.0-μm calculations due to the contribution of reflected solar radiation and the more complex shape of the scattering phase function. Daytime calculations were performed for a cloud composed of two different hexagonal ice crystals ($L/2a$ = 20/20 and 300/100) using the truncated hexagonal ice crystal phase function fit. The oscillatory nature of the 3.7-μm brightness temperature error is due to the behavior of the Legendre fit of the truncated phase function for the specific scattering geometry of the simulation (119° scattering angle) and the numerical method of solution. For the 32+ term solutions, the error in the 3.7-μm temperature calculation is less than approximately 0.4 K for both small and large particles with the geometry specified. The larger particle has larger error fluctuations, indicative of a more significant convergence problem, that is, a stronger dependence on the scattering and absorption behavior. The behavior at other viewing geometries is similar, though the error fluctuations (~0.1 K) are damped if one considers the rms error over scattering angles greater than approximately 30° only. The primary conclusion, however, is that the 32-

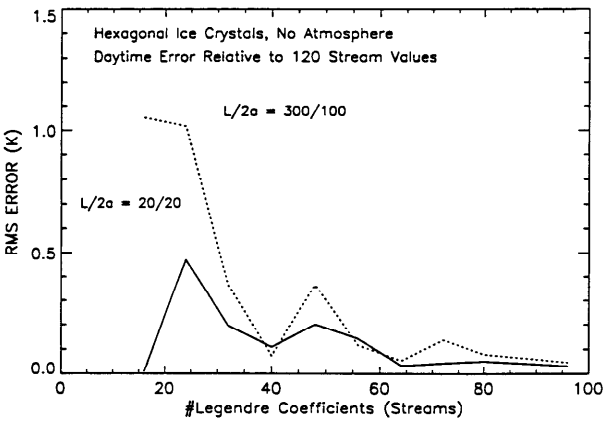

FIG. 4. Daytime rms error in the 3.7-μm brightness temperature ($T_{3.7}$) values versus the number of streams used in the calculations for two particle sizes. The rms errors are calculated relative to the 120-stream results (over a range of cloud optical depths), and the number of streams equals the number of Legendre coefficients used to fit the scattering phase function.

term fit produces consistently reliable results with rms errors less than 0.5 K.

d. Equivalent radius definition

The literature (Takano et al. 1992; Asano and Sato 1980; Pollack and Cuzzi 1980) cites the use of equivalent volume spheres to best conserve the single-scatter albedo of ice hexagons, and the use of equivalent surface area spheres to best conserve the extinction cross section. To test the effects of these approximations, we determine both equivalent volume and equivalent surface area spherical radii. Using the conservation of single-scatter albedo, we attempt to conserve the absorption and scattering characteristics of the hexagons for the NIR and IR regimes.

The effective size parameter ($\chi_{\text{eff}} = 2\pi R_e/\lambda$) generally governs the choice of an equivalent volume or equivalent surface area approach. Pollack and Cuzzi (1980) use a critical size parameter χ_0 to parameterize the difference between large and small particle behavior, where χ_0 is dependent on the imaginary component of the refractive index m_i and the shape and size of the particle. Pollack and Cuzzi (1980) conclude that when one considers the phase function and efficiencies for particles with $\chi_{\text{eff}} < \chi_0$ and the absorption efficiency for particles with $\chi_{\text{eff}} > \chi_0$ (or $2\chi_{\text{eff}} m_i < 1$), equal volume spheres are appropriate. However, when considering the scattering efficiency and diffraction pattern of particles with $\chi_{\text{eff}} > \chi_0$ (or $2\chi_{\text{eff}} m_i > 1$), equal area spheres are considered appropriate. We first elect to show the equivalent volume approach; the equivalent surface area effective radius then simply follows.

Formally, the particle absorption or coalbedo α is given by $\alpha = 1 - \omega_0$, where ω_0 is the single-scatter albedo ω_0 for a distribution of particles. The single-scatter albedo is defined as

$$\omega_0 = \frac{\int Q_{\text{scat}}\sigma(r')n(r')dr'}{\int Q_{\text{ext}}\sigma(r')n(r')dr'}, \qquad (1)$$

where Q_{scat} and Q_{ext} are the scattering and extinction efficiencies, r' is the particle size, $\sigma(r')$ is the geometrical cross section, and $n(r')$ is the number density in the particle size range r' to $r' + dr'$. The extinction efficiency is the sum of the absorption and scattering efficiencies: $Q_{\text{ext}} = Q_{\text{scat}} + Q_{\text{abs}}$. In the large particle limit $\chi_{\text{eff}} \gg 1$, the extinction efficiency $Q_{\text{ext}} \approx 2$. Further, in the limit of moderate to weak absorption (valid in the IR and NIR for the particle sizes considered) $Q_{\text{abs}} \approx kr'$, where k is a constant. Using these assumptions, we can define an "effective radius";

$$R_e = \frac{\int r'\sigma(r')n(r')dr'}{\int \sigma(r')n(r')dr'}, \qquad (2)$$

where r' and $\sigma(r')$ are determined from the particle size distribution and shape.

Since absorption is dominant for the wavelengths modeled, the volume (e.g., mass) of the ice particle is more important than either its shape or orientation. Hence, we assume that the ice hexagons are distributed randomly. We then find the equivalent volume radius by equating the volume of a sphere with that of a regular ice hexagon, that is $4/3\pi r^3 = 3a^2L \sin\pi/3$, where L is the length of the hexagonal cylinder, a is the hexagon base radius, and r is the spherical radius. The form of the geometrical particle cross section $\sigma(r')$ depends on the orientation of the hexagons. For a distribution of randomly oriented hexagons, you can use an average extinction cross section $\sigma(r') = A/2$ as per Takano and Liou (1989). Symmetry is assumed, and A, the surface area of a hexagonal cylinder, is $A = 3a^2[\sqrt{3} + 4(L/2a)]$. In this paper, we have considered only a single size distribution of hexagonal crystals; hence, a and L are constants, and the equivalent volume effective radius is simply

$$R_e(\text{volume}) = \left(\frac{9a^2L \sin\pi/3}{4\pi}\right)^{1/3}. \qquad (3)$$

For the aspect ratios ($L/2a$) given in Takano and Liou (1989), the equivalent volume effective radii are given in Table 1.

To determine the equivalent surface area radius, we replace the equal volume assumption with an equal surface area assumption; for example, $4\pi r^2 = 3a^2[\sqrt{3} + 4(L/2a)]$. We again assume symmetry, and the variables are as defined as before. For a distribution of randomly oriented hexagons of uniform size, the expression for the effective radius of a equivalent surface area is

$$R_e(\text{surface area}) = \left(\frac{3\sqrt{3}a^2 + 6aL}{4\pi}\right)^{1/2}. \qquad (4)$$

The equivalent surface area effective radii are provided in Table 1.

4. AVHRR BTD simulations

Figure 5 shows a comparison of the daytime and nighttime AVHRR BTDs for equivalent volume and surface area ice spheres and the corresponding hexagonal ice crystals. Two particle sizes were selected to illustrate the BTD dependence on absorption and scattering efficiency as a function of the size parameter. The BTDs are for a cirrus cloud over a blackbody surface with aspect ratios and effective radii as denoted. The differences between the two spherical approximations are generally small compared to the BTD magnitude, the large-to-small particle contrast (approximately 1 K versus tens of kelvins), and the difference between the hexagon BTDs and the individual spherical BTDs. The BTD signature of clouds com-

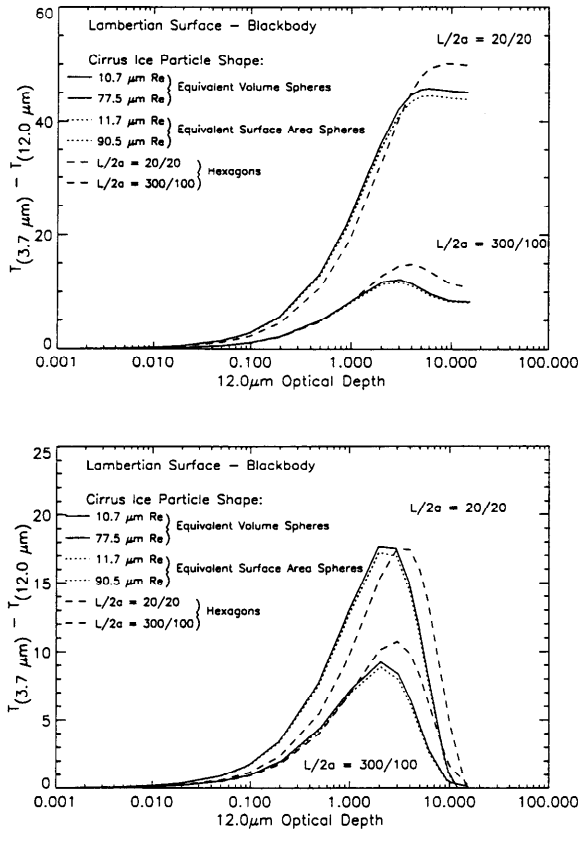

FIG. 5. (a) Daytime and (b) nighttime AVHRR BTD ($T_{3.7} - T_{12.0}$) signatures for cirrus composed of randomly oriented ice hexagons and equivalent ice spheres over a black surface with no intervening atmosphere. Two different ice hexagon particle size BTD signatures are compared to equivalent volume and surface area ice sphere results (see Table 1).

posed of randomly oriented hexagonal ice crystals is significantly different from that of a cloud composed of equivalent ice spheres (volume or surface area), particularly for optically thick clouds. The following sections discuss these differences in more detail.

a. Spherical ice particles

Figure 5 shows a comparison of the daytime and nighttime BTD signatures for ice spheres versus ice hexagons for the AVHRR 3.7- and 12.0-μm channels. The incident solar intensity used for the 3.7-μm AVHRR NIR channel is 4.055 W m^{-2} sr^{-1} (Iqbal 1983, Table C.1). The model conditions are otherwise the same as those cited for Fig. 1. The brightness temperature difference between the AVHRR NIR–IR channels is dependent on particle size and is defined as BTD = $T_{3.7} - T_{12.0}$.

As shown in Fig. 5 (and Fig. 1 for VAS), the daytime BTD signatures for cirrus composed of ice spheres have high BTD values (>30–40 K) for small particles (R_e < 16 μm). Particles of all sizes demonstrate an asymptotic BTD limit with large cloud extinction optical depth $\delta_c \gtrsim 10$. At night, the BTD values increase with cloud optical depth to a peak value when $\delta_c \sim 2$–3, where the cloud emissions become dominant. This small-to-large particle contrast and the BTD magnitude is the diurnally dependent BTD signature. The contrast in daytime BTDs between cirrus composed of small versus large ice crystals ranges from 40 to 55 K for optical depths $2 \lesssim \delta_c \lesssim 5$, while the contrast for nighttime BTDs is approximately 10 K for the same range of optical depths.

Neither equivalent sphere (volume or surface area) accurately mimics the scattering or absorption properties of a distribution of randomly oriented ice hexagons. The ice spheres overestimate the BTDs for optically thin clouds and underestimate the BTDs for the optically thick clouds. This BTD behavior of equivalent spheres is most easily observed for two limiting cloud optical depths ($\delta_c \lesssim 1$ and $\delta_c \gtrsim 10$) and is more evident for small particles, such as the daytime $L/2a = 20/20$ case in Fig. 5a. In this case, ΔBTD ≈ 4–5 K for $\delta_c \sim 1$ and ΔBTD ≈ 5–6 K for $\delta_c \sim 10$, where ΔBTD is defined as $|\mathrm{BTD}_{\mathrm{hexagon}} - \mathrm{BTD}_{\mathrm{sphere}}|$.

The choice of equivalent sphere (volume or surface area) is insignificant compared to the hexagonal crystal BTD signature when only the IR components are considered (nighttime cases). For the nighttime $L/2a = 20/20$ case, ΔBTD ≈ 3 K for $\delta_c \sim 3$ and ΔBTD ≈ 4 K for $\delta_c \sim 10$. The primary problem apparent from Fig. 5b is the shift in the peak BTD values to larger extinction optical depth (from $\delta_c \approx 2.0$ to $\delta_c \approx 3.0$). There is an identical shift in the daytime BTD simulations (Fig. 5a); it is just not as obvious due to the shape of the BTD signature. This shift in BTD is easily explained. The extinction cross sections (hence, optical depths) of ice hexagons (see Table 1) are larger than those of equivalent ice spheres, while the single-scatter albedos of ice hexagons are smaller than those of equivalent ice spheres. Overestimation of δ_c and underestimation of ω_0 results in an apparent increase in absorption by the cloud, which causes an increase in BTD for optically thin clouds and a BTD peak shift.

b. Hexagonal ice crystals

Figure 6 provides examples of BTD signatures for cirrus clouds composed of randomly oriented hexagonal ice crystals of different sizes over a blackbody surface. The model calculations are performed for single particle size distributions characterized by the aspect ratios given in Table 1. Since a 12.0-μm ice hexagon phase function was not available, the 10.8-μm hexagonal ice crystal phase functions (Minnis et al. 1993) were used as first-order 12.0-μm functions. For hexagons that satisfy the large particle approximation ($\chi_{\mathrm{eff}} \gtrsim 30$), the single-scatter albedos used in the calculations were generated from expressions for the extinction and

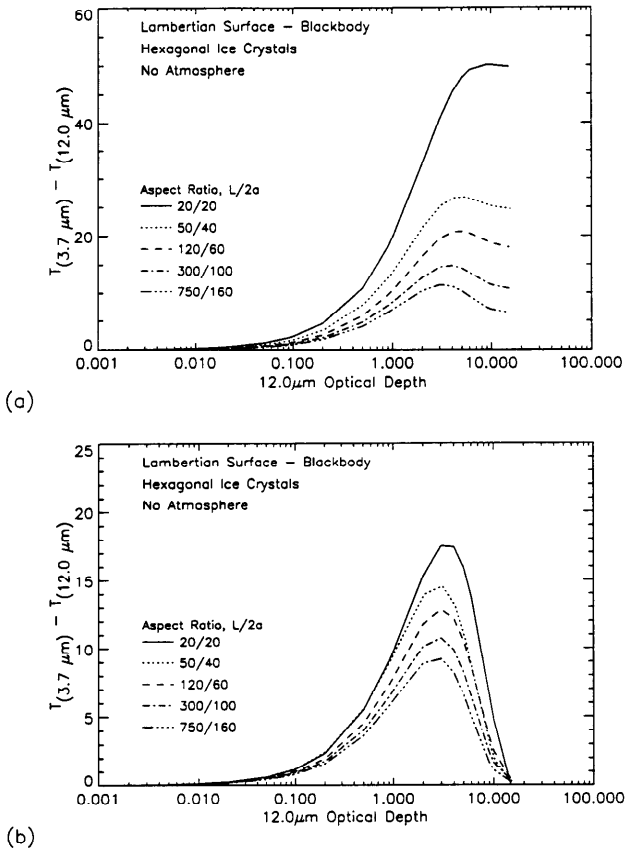

FIG. 6. (a) Daytime and (b) nighttime AVHRR BTD signatures for cirrus composed of randomly oriented ice hexagons over a black surface with no intervening atmosphere.

scattering cross sections from Takano and Liou (1989). For small hexagonal crystals ($\chi_{\text{eff}} < 30$), where ray-tracing techniques cannot be used to determine optical properties, the small particle parameterization of Takano et al. (1992) is used. Takano et al. (1992) suggested the use of spheroids (oblate and prolate) to model the behavior of randomly oriented hexagonal ice crystals. We have used an analogous approach, the composite sphere (see the next section). The optical properties for the hexagonal ice crystals are provided in Table 1.

Comparison of the daytime BTD values for hexagonal ice crystals with the values for ice spheres (Fig. 5) shows that the BTD contrast between small (R_e = 10.7 μm or $L/2a$ = 20/20) and large (R_e = 77.5 μm or $L/2a$ = 300/100) particles is greater for optically thick clouds composed of hexagonal crystals, and less for optically thin clouds. The contrast in daytime BTDs between cirrus composed of small versus large hexagonal ice crystals ranges from 15 to 50 K for optical depths $2 \leqslant \delta_c \leqslant 5$, while at night the contrast in BTDs is approximately 10 K for the same range of optical depths.

5. Use of composite ice spheres

a. Comparison to hexagons and equivalent spheres

While performing the equivalent ice sphere versus ice hexagon simulations and comparisons, a question arose: Can one use an ice sphere to accurately reproduce the BTD signature of an ice hexagon? Intuitively, there is no indication that this approach will work since the single-scatter albedos and extinction optical depths are incorrectly estimated by means of equivalent ice sphere approximations. Further, the ice sphere (Mie) and Henyey–Greenstein phase functions do not truly represent the more complex scattering behavior of the hexagonal ice crystals. However, if one blithely ignores these difficulties, an option arises. Namely, the construction of equivalent "composite" spheres to model ice hexagons.

To first order, the ω_0 values for equivalent volume spheres best approximate the ice hexagon ω_0 values, while equivalent surface area sphere σ_{ext} values best approximate the σ_{ext} values of ice hexagons. We proposed a test: build a "composite" sphere incorporating these two features, pick a scattering phase function, and perform BTD simulations. Figure 7a shows the daytime BTD signatures that result for a small particle ($L/2a$ = 20/20) simulation. The solid curve is the ice hexagon BTD signature; the others represent different composite sphere simulations, where the scattering phase function is variable, as noted. The use of a composite sphere with a hexagonal crystal phase function provides the closest comparison to the actual hexagon BTD. A composite sphere with an equivalent volume ice sphere (Mie) phase function gives the best result of the spherical scattering phase functions. Comparison of Figs. 5a and 7a shows that for $\delta_c \leqslant 3$ the composite sphere is a better approximation than either equivalent sphere with an approximate 50% reduction in ΔBTD (ΔBTD ⩽ 3 K, < 10% of the BTD magnitude). The composite sphere produces the proper BTD peak and comparable BTDs for $\delta_c \geqslant 6$, that is, ΔBTD ≈ 6–8 K for the composite sphere versus ΔBTD ≈ 4–7 K for the equivalent spheres.

Figure 7b shows the results of the nighttime BTD simulation of the $L/2a$ = 20/20 case with the composite sphere. Comparison of Figs. 5b and 7b indicates that the composite sphere versus hexagon BTDs show better agreement than the equivalent sphere versus hexagon comparison. The composite sphere plus hexagonal ice crystal phase function again provides the best comparison over all cloud optical depths. The peak BTD is not well modeled for composite spheres with the equivalent ice sphere (Mie) scattering phase functions. For large optical depths ($\delta_c \geqslant 4$), the composite sphere BTDs reproduce the ice hexagon BTDs quite well. There is generally a factor-of-2 decrease in ΔBTD when composite spheres, rather than equivalent spheres, are used to represent ice hexagons.

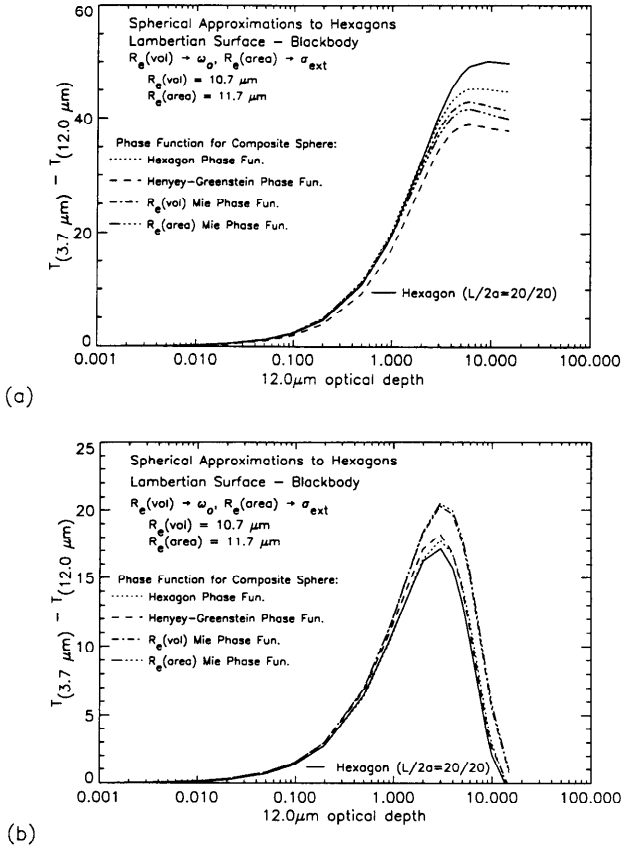

FIG. 7. Comparison of the (a) daytime and (b) nighttime AVHRR BTD signatures for a cirrus composed of randomly oriented ice hexagons (solid line) and a composite sphere with different scattering phase functions.

Several interesting points rise from the use of a composite sphere. First, since the effects of randomly oriented ice hexagons on BTDs are more accurately modeled by means of composite spheres than by equivalent spheres, the next step is to explore the application of composite spheres to more complex nonspherical particles (dendrites, bullet, rosettes, etc.). Second, the availability of nonspherical particle optical properties is limited, particularly as regards the scattering phase functions. This is a problem if one hopes to use satellite information to estimate particle sizes. Use of composite spheres to mimic optical properties of nonspherical particles is, therefore, useful. Further work is in progress to compare the intuitively similar results of composite spheres and spheroids (Takano et al. 1992; Bohren and Huffman 1983). We expect that the approaches will produce similar results, though the determination of equivalent radii for accurate comparison of spheroids and composite spheres is a bit problematic.

b. *Particle size estimates from BTDs*

The dependence of BTD on particle size is fairly simple to determine if one uses spherical particles. Since the BTD signatures approach a limit as the size of the particle increases, the sensitivity of BTD to particle size for a specific cloud optical depth must also have bounds. We use composite spheres to approximate the optical behavior of ice hexagons by determining ω_0 and δ_c as described previously and then rely on the fact that the scattering phase function varies slowly with particle size (aspect ratio). We select the ice hexagon phase function with the closest size and then vary the size of the composite sphere to simulate BTDs; this establishes the BTD dependence on R_e for particles with radii between about 10 and 150 μm. Calculations using composite spheres indicate that a 5-K change in daytime BTD for large optical depths ($\delta_c \gtrsim 3$) translates into a 5–6-μm change in R_e. Equivalently, at night, a 5–6-μm change in R_e translates into an approximate 1.5-K shift in peak BTD, or ΔBTD. We define ΔBTD as the absolute difference between the ice hexagon result and the composite sphere results with different scattering phase function; for example, $\Delta\text{BTD} = |\text{BTD}_{\text{hexagon}} - \text{BTD}_{\text{composite}}|$. The ability to translate ΔBTD into ΔR_e is very useful, since there are only a discrete number of hexagonal crystal phase functions available in the literature (Takano and Liou 1989). The translation of ΔBTD to ΔR_e holds even when ice hexagon scattering information is not available. Figure 7 illustrates this point. In the large optical depth limit, Fig. 7a indicates that the daytime ΔBTDs vary from 6 to 15 K, depending on the phase function selected. This implies that effective radii can be estimated during the day to within about 15 μm at worst, and to within about 5 μm at best. Figure 7b indicates that ΔBTD varies from 1 to 4 K at night for peak BTD values ($\delta_c \sim 3$), which implies that effective radius estimates are also within about 5–15 μm at night. This consistency is encouraging and can be attributed to the dominance of absorption at the NIR and IR wavelengths used in our analysis. Further work must be done to study and apply these results, with special attention to the dependence of BTDs on scattering angle.

6. BTD dependence on surface and view angles

a. *Surface reflectance and atmosphere*

To more accurately estimate the particle size BTD dependence under realistic conditions, it is necessary to account for the effects of a nonblack surface. The effects of a thin cirrus composed of small, randomly oriented hexagonal ice crystals ($L/2a = 20/20$) over different Lambertian surfaces (hemispheric reflectance, ρ_s) on BTDs are given in Fig. 8 for day and night. Black ($\rho_s = 0\%$) and nonblack ($\rho_s \neq 0\%$) surfaces are considered. BTDs are provided for a variety of surface types (quartz sand, seawater, deciduous vegetation, and smooth sea ice) with reflectance information from Salisbury and D'Aria (1992, 1994). The NIR and IR surface reflectances for the four surface types cited are given in Fig. 9 with satellite channels annotated. For

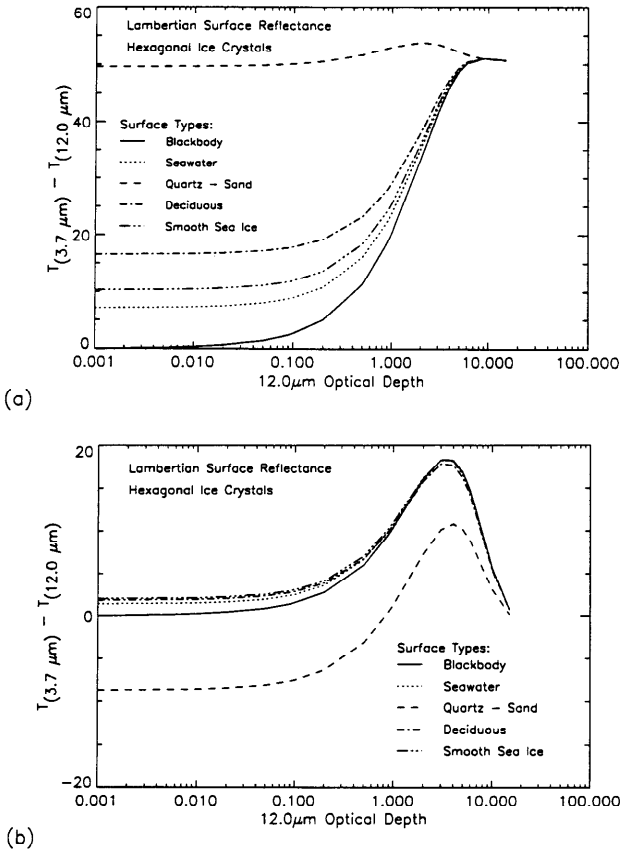

FIG. 8. (a) Daytime and (b) nighttime AVHRR BTD signatures for cirrus composed of randomly oriented hexagonal ice crystals over different Lambertian surface types.

optically thin clouds ($\delta_c \leqslant 1$), the range of daytime BTDs for most surface types is about 6–15 K, as indicated by Fig. 8a. The spectral signature of quartz carbonate bands (Fig. 9) significantly influences the reflectance and emissivity of the surface. Figure 8a shows that the reflectivity of quartz sand has a significant effect on the daytime BTD signature due to the contribution of reflected solar radiation at 3.7 μm. The BTD contrast between thin clouds over sandy surfaces (quartz) and thin clouds over other surface types is significant ($\geqslant$25 K). At night, the range of BTDs for most surface types is less than approximately 2 K as indicated in Fig. 8b. For sandy (quartz) surfaces, the BTD signature again shows a distinct and significant ($\sim$8 K) difference, even for optically thick clouds ($\delta_c \geqslant 4$). This is due to the nonblack surface emittance. That is, for quartz sand the emittance ($1 - \rho_s$) is approximately 0.5.

The effects of a realistic clear-sky atmospheric profile were considered but are not completely resolved. For optically thin clouds, it is important to determine the clear-sky background effects, particularly in the NIR and IR. We are in the process of computing clear-sky optical depth profiles for the AVHRR 3.7-, 10.8-, and 12.0-μm channels, among others. To facilitate our study, we are comparing the results of a line-by-line radiative transfer model (Kratz et al. 1991; Schmidt et al. 1993) with the DISORT band model (Stamnes et al. 1988). A correlated k-distribution method similar to that of Fu and Liou (1992) is the basis for efforts to evaluate the spectral line overlap problem and its effects on NIR and IR optical depth profiles for finite band models.

b. *View-angle effects*

Figure 10 illustrates the effect of view zenith angle on the diurnal BTD signatures. A cirrus cloud composed of small hexagonal ice crystals ($L/2a = 20/20$) at 245 K over a black surface at 289 K is assumed. For optically thin clouds, the solar zenith angle θ_0, satellite view zenith angle θ, and satellite view azimuth angle ϕ can be used to determine which portion of the scattering phase function dominates the radiative transfer calculations used to simulate AVHRR or GOES ra-

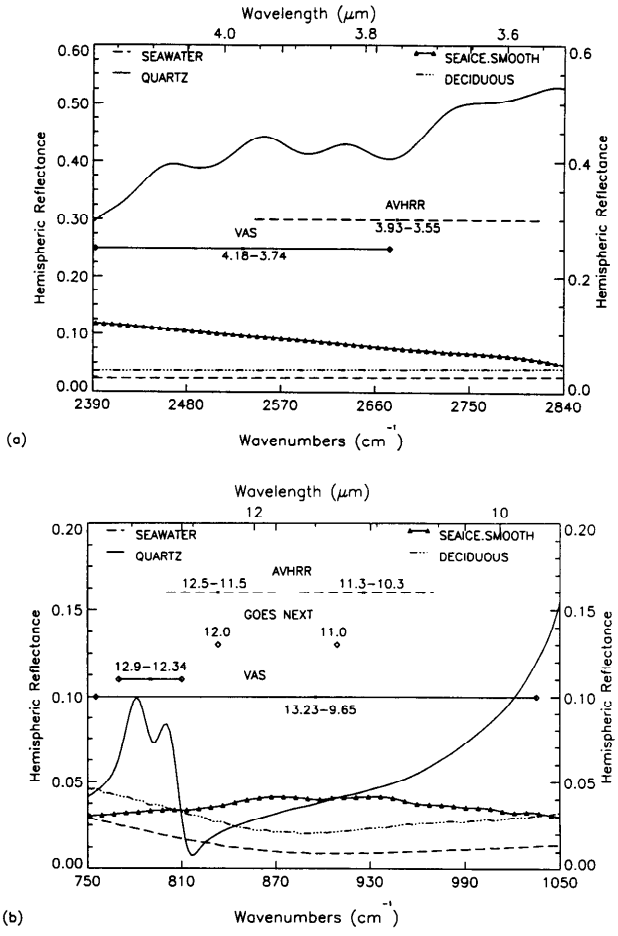

FIG. 9. Hemispheric reflectances of different surface material in the (a) 3.7-μm and (b) 10–12-μm window (from Salisbury and D'Aria 1992, 1994). Different satellite channels are indicated.

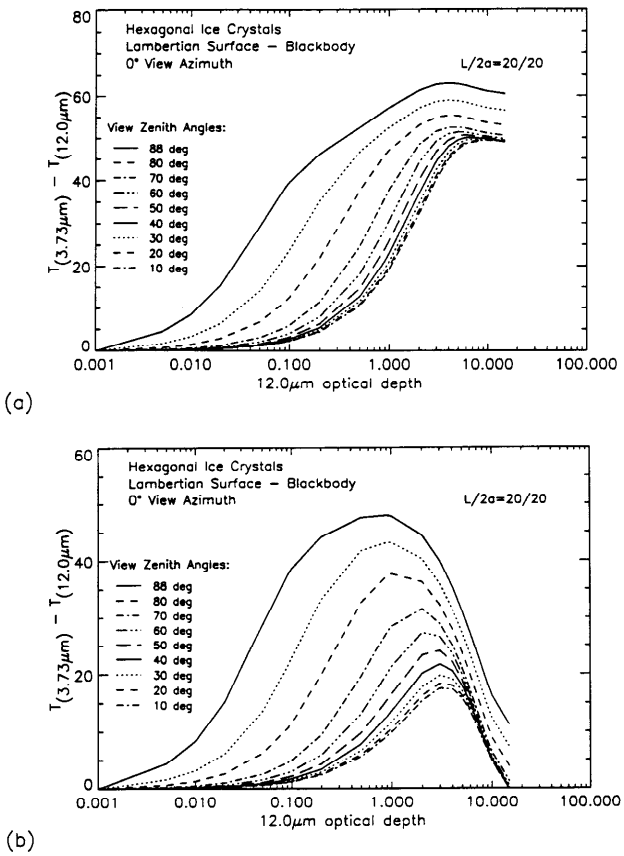

FIG. 10. Dependence of the (a) daytime and (b) nighttime AVHRR BTD signature on view zenith angle for a cirrus composed of randomly oriented ice hexagons over a black surface with no intervening atmosphere.

diances. For the example, in Fig. 10, given solar zenith angle ($\theta_0 = 24°$) and satellite view azimuth ($\phi = 0°$), the corresponding scattering angle for the phase function η is simply $\eta = 180° - \theta_0 - \theta = 156° - \theta$. AVHRR view zenith angles θ between 0° and 60° correspond to η between 156° and 96°.

As Fig. 10 shows, top-of-the-atmosphere (TOA) BTDs at all cloud optical depths are significantly affected when view zenith angles are greater than approximately 60°. This is particularly true for optically thin clouds ($\delta_c \leqslant 0.5$). This is due primarily to limb effects on the NIR and IR BTD signatures when viewing cirrus over a hot surface. In the IR window, superposition of a cold cloud over a hot surface will cause limb darkening. (For example, as the pathlength through the cirrus increases with an increase in θ, the apparent surface brightness temperature will decrease.) In the NIR, the superposition of a cirrus cloud will have different effects during the day versus night. At night, a cirrus will cause limb darkening in the NIR, though the magnitude of the darkening is less than that seen in the IR window. During the day, the presence of the cirrus will actually cause limb brightening at 3.7 μm, or an increase in the apparent surface brightness temperature. The limb brightening is due to the reflection of incident solar radiation by the ice crystals in the cirrus cloud. In both daytime and nighttime cases, the pathlength through the cloud increases with $\cos\theta$, and the limb effects consequently increase with view zenith angle. Since the apparent brightness temperatures in the NIR either increase or decrease slowly compared to the IR values, the BTDs increase as the view zenith angles move away from nadir.

We have not considered the effects of the sphericity of the atmosphere or horizontal cloud inhomogeneities that would mitigate some of the TOA BTD dependence on view zenith. However, these effects are expected to be small in comparison with the magnitude of the BTD signatures for $\theta \leqslant 80°$. Beyond about 80°, the plane-parallel approximation begins to break down, which means that model BTDs will become highly nonlinear functions of $\cos\theta$. The BTDs for view zenith angles less than 40° show only a slight dependence on $\cos\theta$, as expected, since limb effects are minimized by small changes in the optical paths. The increase in cirrus BTD magnitude for view zenith angles greater than 60° agrees with prior analysis of the effects of optically thin cirrus on the radiometric profile of the upper troposphere (Schmidt et al. 1990).

7. Conclusions

Effective cirrus cloud particle size discrimination from satellite data is theoretically possible, if the IR extinction optical depth of the cloud can be determined and the NIR–IR BTD values measured. Generally, complications arise because of the broad range of particle sizes and shapes that compose cloud composition. We have considered only randomly oriented hexagonal ice crystals and ice spheres, ignoring bullets, rosettes, dendrites, and other crystal types commonly found in cirrus clouds (Heymsfield and Platt 1984). BTD simulations provide a means to combine radiative transfer modeling and observational data analysis of cirrus clouds. The use of NIR–IR BTD signatures to bound cloud ice particle size estimates as derived from satellite-borne radiometers appears reasonable for optical depths (δ_c) greater than approximately 1 during the day and $1 \leqslant \delta_c \leqslant 6$ at night.

The rms error in the brightness temperatures calculated and the NIR–IR BTD signatures are sensitive to the number of Legendre coefficients used to fit the scattering phase function. The effectiveness of truncation is highly dependent on the delta-function nature of the forward-scattering peak and the complexity of the phase function. For ice hexagon and ice sphere phase functions with large asymmetry factors ($g \geqslant 0.85$), Legendre polynomial fits to the truncated phase functions can be done with less than approximately 20% rms error over all scattering angles with 50 coefficients or fewer. The simulation geometry may

limit the usefulness of truncation, particularly if halo or solar aureole effects are to be modeled, and the relative error of the Legendre fit at specific scattering angles of interest must be considered.

The BTD signature of a cirrus cloud composed of equivalent ice spheres (volume or surface area) is different from the BTD signature of a cirrus composed of randomly oriented ice hexagons. The difference is due to the fact that equivalent spheres overestimate single-scatter albedo ω_0 and underestimate cloud extinction optical depth δ_c. For daytime simulations, use of equivalent sphere models generates BTDs that are in error by 4–6 K for $1 \leqslant \delta_c \leqslant 6$, while the use of the composite spheres reduces the error by a factor of 2. For the nighttime simulations, the composite sphere model also approximately halves the BTD error (from 2–4 to 1.5–2 K) for the same range of cloud optical depths. Composite sphere model simulations also produce peak BTD values at the correct optical depths. Use of composite spheres to model more complex ice crystals is promising as the variation of BTD with particle size is easily determined. Further study is required to establish limits on the use of composite spheres, particularly as an approximation to other types of nonspherical particles. Comparison of the effects of composite spheres to those of spheroids is planned to determine the validity of the solution.

The reflectance properties of all nonblack surfaces are important, particularly as regards the particle size contrast in BTDs for optically thin clouds. The simulations for a cirrus cloud composed of hexagonal ice crystals over a quartz sand surface indicate that the surface reflectance dominates the BTD for cloud optical depths $\delta_c \leqslant 6$. Detection and characterization of cirrus clouds over desert is known to be difficult; our results confirm that fact. Surface reflectance contributions from seawater, smooth sea ice, and deciduous vegetation dominate the BTD signatures of thin cirrus clouds ($\delta_c \leqslant 1.0$) during the day. At night, the cloud-top temperature controls BTDs for optically thick cirrus ($\delta_c \geqslant 4$) above most surface types (other than quartz sand); nonblack surface emissions contribute for $\delta_c \leqslant 3$.

View zenith angle effects on the BTD signatures indicate that for view zenith angles $\theta \leqslant 40°$ the BTD signatures are minimally affected. However, for larger view zenith angles $\theta \geqslant 60°$, the BTD signatures depart significantly from the nominal case due to limb effects. For $\theta \geqslant 80°$, the plane-parallel approximation also begins to break down, so care must be taken when comparing model BTDs to satellite observations at large view zenith angles.

Acknowledgments. We wish to thank NASA Langley Research Center for their support. The LaRC Atmospheric Science Division, Lockheed Engineering and Science Company, and the NOAA Climate Monitoring and Diagnostics (CMDL) Laboratory also provided support for analysis and modeling efforts. We also wish to thank Drs. Y. Takano, K.-N. Liou, and P. Minnis for providing the 3.7- and 10.8-μm hexagonal ice crystal phase functions, and Drs. Salisbury and D'Aria for the surface reflectance database. David Bailey assisted with the preparation of figures for the manuscript.

REFERENCES

Asano, S., and M. Sato, 1980: Light scattering by randomly oriented spheroidal particles. *Appl. Opt.*, **19,** 962–974.

Baum, B. A., B. A. Weilicki, P. Minnis, and L. Parker, 1992: Cloud property retrieval using merged HIRS/2 and AVHRR data. *J. Appl. Meteor.*, **31,** 351–369.

Bohren, C. F., and D. R. Huffman, 1983: *Absorption and Scattering of Light by Small Particles.* John Wiley & Sons, 530 pp.

Coakley, J. A., Jr., and R. P. Bretherton, 1982: Cloud cover from high resolution scanner data: Detecting and allowing for paritally filled fields of view. *J. Geophys. Res.*, **87,** 4917–4932.

Fu, Q., and K. N. Liou, 1992: On the correlated *k*-distribution method for radiative transfer in nonhomogeneous atmospheres. *J. Atmos. Sci.*, **49,** 2139–2156.

Hansen, J. E., 1971: Multiple scattering of polarized light in a planetary atmosphere. Part II: Sunlight reflected by terrestrial water clouds. *J. Atmos. Sci.*, **28,** 1400–1426.

Heymsfield, A. J., and C. M. R. Platt, 1984: A parameterization of the particle size spectrum of ice clouds in terms of the ambient temperature and the ice water content. *J. Atmos. Sci.*, **41,** 846–855.

Inoue, T., 1987: A cloud type classification with *NOAA-7* split-window measurements. *J. Geophys. Res.*, **92,** 3991–4000.

Iqbal, M., 1983: *An Introduction to Solar Radiation.* Academic Press, 390 pp.

Kratz, D. P., B.-C., Gao, and J. T. Kiehl, 1991: A study of the radiative effects of the 9.4- and 10.4-micron bands of carbon dioxide. *J. Geophys. Res.*, **96,** 9021–9026.

Minnis, P., E. F. Harrison, and G. G. Gibson, 1987: Cloud cover over the eastern equatorial Pacific derived from July 1983 ISCCP data using a hybrid bispectral threshold method. *J. Geophys. Res.*, **92,** 4051–4073.

——, K.-N., Liou, and Y. Takano, 1993: Inference of cirrus cloud properties using satellite-observed visible and infrared radiances. Part I: Parameterization of radiance fields. *J. Atmos. Sci.*, **50,** 1279–1304.

Platt, C. M. R., 1983: On the bispectral method for cloud parameter determination from satellite VISSR data: Separating broken cloud and semitransparent cloud. *J. Climate Appl. Meteor.*, **22,** 429–439.

——, and A. C. Dilley, 1979: Remote sounding of high clouds. Part I: Calculation of visible and infrared optical properties from lidar and radiometer measurements. *J. Appl. Meteor.*, **18,** 1130–1143.

Pollack, J. B., and J. N. Cuzzi, 1980: Scattering by nonspherical particles of size comparable to a wavelength: A new semi-empirical theory and its application to tropospheric aerosols. *J. Atmos. Sci.*, **37,** 868–881.

Potter, J. F., 1970: The delta function approximation in radiative transfer theory. *J. Atmos. Sci.*, **27,** 943–949.

Prabhakara, C., R. S. Fraser, G. Dalu, M.-L. C. Wu, and R. J. Curran, 1988: Thin cirrus clouds: Seasonal distribution over oceans deduced from Nimbus 4 IRIS. *J. Appl. Meteor.*, **27,** 379–399.

Rossow, W. B., F. Mosher, E. Kinsella, A. Arking, M. Desbois, E. Harrison, P. Minnis, E. Ruprecht, G. Seze, C. Simmer, and E. Smith, 1985: ISCCP cloud algorithm intercomparison. *J. Climate Appl. Meteor.*, **24,** 877–903.

Salisbury, J. W., and D. M. D'Aria, 1992: Emissivity of terrestrial materials in the 8–14 μm atmospheric window. *Remote Sens. Environ.*, **42,** 83–106.

——, and ——, 1994: Emissivity of terrestrial materials in the 3–5 μm atmospheric window. *Remote Sens. Environ.*, **47,** 345–361.

——, E. M. Patterson, and W. J. Williams, 1990: Influence of high altitude clouds on upper tropospheric radiance measurements. *Appl. Opt.*, **29,** 4199–4207.

Schmidt, E. O., 1991: Cloud properties as inferred from HIRS/2 multi-spectral data. Ph.D. dissertation, Georgia Institute of Technology, 145 pp.

——, D. P. Kratz, and B. A. Wielicki, 1993: Effects of cirrus clouds and the atmosphere over land and ocean surfaces. *Proc. Int. Geosci. and Remote Sens. Symp.*, **3,** 1107–1112.

Sobolev, V. V., 1978: *A Treatise on Radiative Transfer.* D. Van Nostrand Co., Inc., 239 pp.

Stamnes, K., S.-C. Tsay, W. Wiscombe, and K. Jayaweera, 1988: Numerically stable algorithm for discrete-ordinate-method radiative transfer in multiple scattering and emitting layered media. *Appl. Opt.*, **24,** 2502–2509.

Stephens, G. L., and S.-C. Tsay, 1990: On the cloud absorption anomaly. *Quart. J. Roy. Meteor. Soc.*, **116,** 671–704.

Stone, R. S., G. L. Stephens, C. M. R. Platt, and S. Banks, 1990: The remote sensing of thin cirrus cloud using satellites, lidar and radiative transfer theory. *J. Appl. Meteor.*, **29,** 353–366.

Takano, Y., and K.-N. Liou, 1989: Solar radiative transfer in cirrus clouds. Part I: Single-scattering and optical properties of hexagonal ice crystals. *J. Atmos. Sci.*, **46,** 3–19.

——, ——, and P. Minnis, 1992: The effects of small ice crystals on infrared radiative properties. *J. Atmos. Sci.*, **49,** 1487–1493.

Tsay, S.-C., G. L. Stephens, and T. J. Greenwald, 1991: An investigation of aerosol microstructure on visual air quality. *Atmos. Environ.*, **25A,** 1039–1053.

Welch, R. M., S. K. Sengupta, and D. W. Chen, 1988: Cloud field classification based upon high spatial resolution textural features. 1: Gray level co-occurrence matrix approach. *J. Geophys. Res.*, **93,** 12 663–12 681.

Wiscombe, W. J., 1977: The delta-M method: Rapid yet accurate radiative flux calculations for strongly asymmetric phase functions. *J. Atmos. Sci.*, **34,** 1408–1422.

——, 1979: Mie scattering calculations: Advances in techniques and fast, vector-speed computer codes. NCAR/TN-140+STR, 29 pp.